

# Deterministic combination of numerical and physical coastal wave models

Haiwen Zhang<sup>a,b,\*</sup>, Hemming A. Schäffer<sup>a,1,2</sup>, Kim P. Jakobsen<sup>a,1</sup>

<sup>a</sup> DHI water and Environment, Agern Alle 5, DK-2970 Hørsholm, Denmark

<sup>b</sup> Department of Mechanical Engineering, Technical University of Denmark, DK-2800 Kgs. Lyngby, Denmark

Received 8 March 2006; received in revised form 9 August 2006; accepted 29 August 2006

Available online 19 October 2006

## Abstract

A deterministic combination of numerical and physical models for coastal waves is developed. In the combined model, a Boussinesq model MIKE 21 BW is applied for the numerical wave computations. A piston-type 2D or 3D wavemaker and the associated control system with active wave absorption provides the interface between the numerical and physical models. The link between numerical and physical models is given by an ad hoc unified wave generation theory which is devised in the study. This wave generation theory accounts for linear dispersion and shallow water non-linearity. Local wave phenomena (evanescent modes) near the wavemaker are taken into account. With this approach, the data transfer between the two models is thus on a deterministic level with detailed wave information transmitted along the wavemaker.

© 2006 Elsevier B.V. All rights reserved.

*Keywords:* Numerical model; Physical model; Wave generation; Active absorption; Non-linear waves; Directional waves

## 1. Introduction

In coastal engineering, numerical models and physical models are two main approaches to study water wave problems. Numerical models are often used for large areas, but they are typically unable to capture highly non-linear physics including wave breaking. Physical models are suitable for simulating complex non-linear processes near the shore or near fixed or floating structures, but they are restricted by the scale and the size of the facility (Oumeraci, 1999). The limited extent of the physical model often prohibits that the offshore boundary is located in sufficiently deep water for the incident waves to be well described by standard, parameterized wave spectra. As this is typically the only available incident wave description, the limited size of the model facility often precludes important local phenomena like refraction and diffraction. The integrated use of

the two approaches could offer an attractive alternative to using either alone. This composite or hybrid modelling has been discussed by Kamphuis (1995, 1996, 2000), Watts (1999), Schäffer (1999) and others.

A suitable combination of numerical and physical models would be a physical model focusing on the complex part of the problem near the shore or near structures and a numerical model for the surrounding wave transformation. Typically, the combination of the two types of models has been to use a numerical model for the determination of wave conditions at the boundary of the physical model. In the traditional approach, the data transfer between the two models is only made on a stochastic level through bulk parameters such as significant wave height and peak period (e.g. Kofoed-Hansen et al., 2000; Gierlevsen et al., 2003). This study aims at a deterministic combination of a numerical and a physical model in two horizontal dimensions. The data transfer between two models will thus include time series of surface elevation and depth-averaged velocity and their variation along the wavemaker. No attempt is made to obtain a two-way coupling, where reflected waves can enter the numerical model from the physical model.

The theory developed for this purpose is referred to as the ad hoc unified wave generation theory. Initial efforts in this

\* Corresponding author. Present address: COWI A/S, Parallelvej 2, DK-2800 Lyngby, Denmark. Fax: +45 4516 9292.

E-mail addresses: [Hazh@cowi.dk](mailto:Hazh@cowi.dk) (H. Zhang), [Hemming@SchafferWaves.dk](mailto:Hemming@SchafferWaves.dk) (H.A. Schäffer), [kpj@dhi.com.my](mailto:kpj@dhi.com.my) (K.P. Jakobsen).

<sup>1</sup> Fax: +45 4516 9292.

<sup>2</sup> Present address: SchäfferWaves, Sortedam Dosserring 59H st., DK-2100 Copenhagen Ø, Denmark.

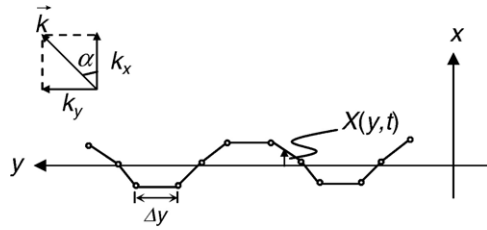


Fig. 1. Horizontal cross-section of 3D wavemaker. Definition sketch.

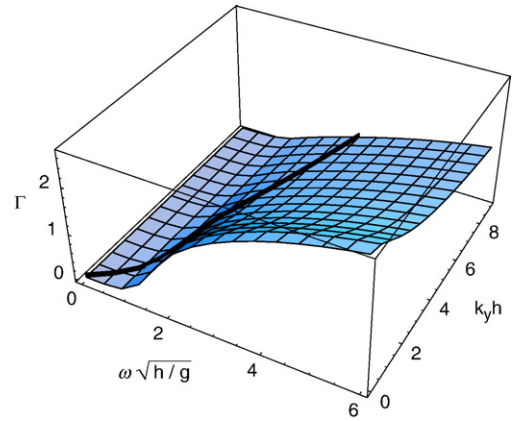


Fig. 3. Transfer function for evanescent-mode correction.

direction include Zhang and Schäffer (2004) for wave flumes, Zhang and Schäffer (2005) for the theoretical aspects in 3D. Furthermore, Zhang and Schäffer (in press) used the ad hoc unified wave generation theory with input from Stream Function wave theory to generate highly nonlinear regular waves of previously unmatched quality. In turn these results provided a validation of the ad hoc theory in 2D.

The ad hoc unified 3D wave generation theory combines 3D linear fully dispersive wavemaker theory (Madsen, 1974, see also Dean and Dalrymple, 1984) and the general wave generation approach for non-linear shallow water waves. The ad hoc theory accounts for shallow water non-linearity and compensates for local wave phenomena (evanescent modes) near the 3D wavemaker. For small amplitude waves, the fully dispersive linear wavemaker theory is recovered. For shallow water waves, it is consistent with non-linear long wave generation. This approach offers a deterministic link between numerical and physical models.

In the combined model, various numerical models or wave theories can be used for the numerical wave computations in the far field. In this study, a Boussinesq model (MIKE 21 BW, Madsen and Sørensen, 1992) is chosen. A Piston-type 2D or 3D wavemaker and the associated control system with active absorption provides the interface between the numerical and physical models. The wavemakers are controlled for simultaneous wave generation and active absorption by an Active Wave Absorption Control System for wave flumes (DHI AWACS) and wave basins (DHI 3D AWACS).

Two different types of wavemaker control are offered by the DHI (3D) AWACS for non-linear wave generation. In *position mode*, the control signal is time series of wavemaker paddle

position. This mode is compatible with the general approach to non-linear wave generation. However active absorption is not included in *position mode*. Another method termed *dual mode* has been developed recently (Schäffer and Jakobsen, 2003; Schäffer, 2001). This allows for active absorption in combination with consistent non-linear wave generation. The active absorption appears as a linear perturbation on the non-linear wave generation. The control signals in *dual mode* are time series of wavemaker paddle position and the corresponding surface elevation at the moving paddle. These two control signals are provided by the ad hoc unified wave generation theory.

In the following, Section 2 outlines the ad hoc 3D unified wave generation theory, while Section 3 and Section 4 provide experimental validation in wave flumes and wave basins, respectively. Section 5 draws up the summary and conclusions.

## 2. Ad hoc 3D unified wave generation theory

Time series of surface elevation, depth-averaged horizontal particle velocity in the  $x$  direction at the wave paddle and paddle position are denoted  $\eta(y,t)$ ,  $U(y,t)$ , and  $X(y,t)$ , respectively, in

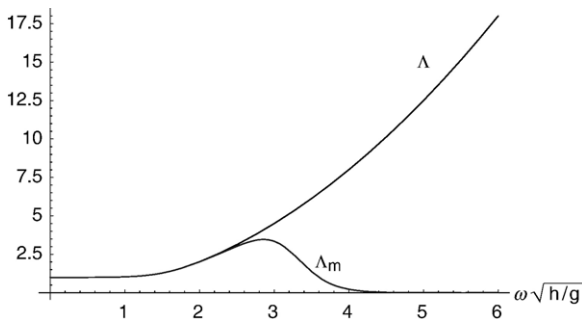


Fig. 2. Transfer function for dispersion correction  $\Lambda$  and modified transfer function  $\Lambda_m$  versus non-dimensional frequency.

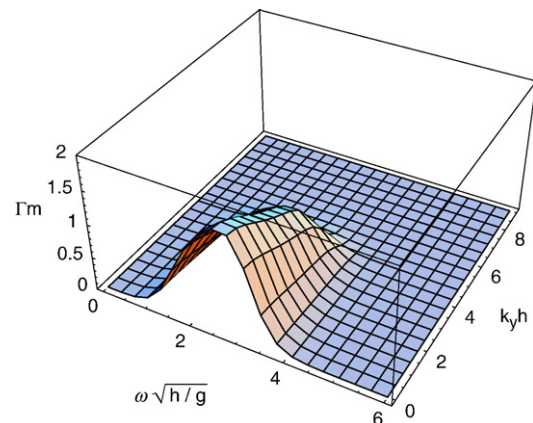


Fig. 4. Modified transfer function for evanescent-mode correction.

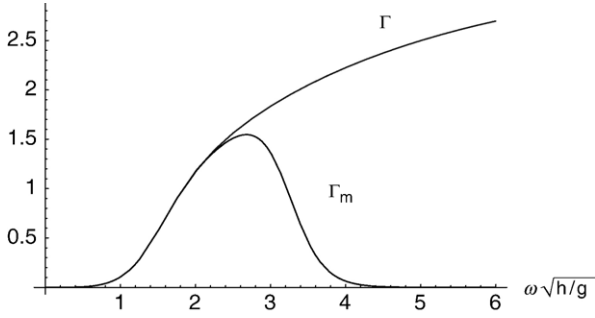


Fig. 5. Transfer functions  $\Gamma_m$  and  $\Gamma$  for normally emitted waves ( $k_y=0$ ).

physical space, while  $A(k_y, \omega)$ ,  $B(k_y, \omega)$  and  $X_a(k_y, \omega)$  denote the equivalent complex Fourier amplitudes:

$$\eta(y, t) \stackrel{\text{2D Fourier Transform}}{\Leftrightarrow} A(k_y, \omega) \quad (1)$$

$$U(y, t) \stackrel{\text{2D Fourier Transform}}{\Leftrightarrow} B(k_y, \omega) \quad (2)$$

$$X(y, t) \stackrel{\text{2D Fourier Transform}}{\Leftrightarrow} X_a(k_y, \omega) \quad (3)$$

Here,  $t$  is time,  $\omega$  is angular frequency, and  $k_y$  is wave number component along the wavemaker. The quantities  $A$  and  $\eta$  carry the following subscripts: "P" for the target, progressive, incident waves, "O" for waves measured at the paddle front, and "I, O" for the expected wave elevation at the front of the moving paddle. Fig. 1 shows a definition sketch of a segmented 3D wavemaker.

### 2.1. Linear wave generation

According to linear fully dispersive 3D wavemaker theory, the paddle position amplitude relates to the progressive wave amplitude as

$$ie_0 X_a = A_I \quad (4)$$

Here,  $i$  is the imaginary unit showing a  $90^\circ$  phase shift, and  $e_0$  is the transfer function defined as

$$e_0 = \frac{1}{\cos \alpha} c_0 \quad (5)$$

Here,  $\alpha$  is the wave propagation direction,  $c_0$  is known as the Biesel transfer function, which for a piston-type wavemaker is given by

$$c_0 = \frac{4 \sinh^2 kh}{2kh + \sinh 2kh} \quad (6)$$

where  $k$  is the wave number and  $h$  is the water depth. As  $B$  denotes the  $x$ -component of the complex amplitude of the depth-averaged velocity of the progressive wave, we have by continuity,

$$B = \frac{\omega}{kh} A_I \cos \alpha \quad (7)$$

In combination with Eqs. (4) and (5), this yields

$$i\omega X_a = AB \quad (8)$$

where

$$A \equiv \frac{kh}{c_0} = \frac{kh(2kh + \sinh 2kh)}{4 \sinh^2 kh} \quad (9)$$

The transfer function  $A$  is shown in Fig. 2. It is independent of the wave direction. Considering the range of applicability of the chosen numerical model Mike 21 BW ( $kh \leq 3$ ,  $\omega \sqrt{h/g} \leq \sqrt{3}$ ), we may damp the high-frequency response by replacing  $A$  with a modified  $A_m$  as shown in Fig. 2.

Eq. (8) may be rewritten as two equations

$$i\omega X_a^{sw}(k_y, \omega) = B(k_y, \omega) \quad (a)$$

$$X_a(k_y, \omega) = A_m X_a^{sw}(k_y, \omega) \quad (b)$$

where superscript "sw" indicates the use of shallow water theory for obtaining the paddle position from the depth-averaged particle velocity at the mean paddle position. Eq. (10b) gives a dispersion correction needed when deviating from the shallow water limit.

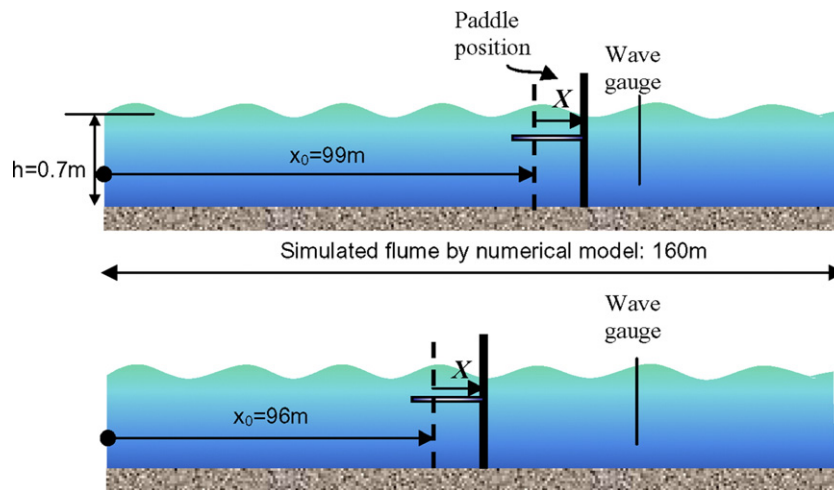


Fig. 6. Sketch of the combined model, using two different mean paddle positions.

The wave paddle position in the time domain can be expressed as

$$\frac{\partial X^{sw}(y, t)}{\partial t} = U(y, t) \tag{11}$$

$$X(y, t) = F^{-1}\{A_m(\omega)F\{X^{sw}(t)\}\} \tag{12}$$

where  $F$  represents the Fourier transform which is evaluated in practice via a Fast Fourier Transform.

For active absorption in *dual mode*, the surface elevation at the moving paddle is furthermore required. Due to the mismatch between the shape of the wave paddle and the vertical profile of the horizontal velocity of progressive waves, an evanescent wave field exists at the paddle front. From linear wavemaker theory, we obtain

$$A_{I,0} = A_I + \Gamma X_a \tag{13}$$

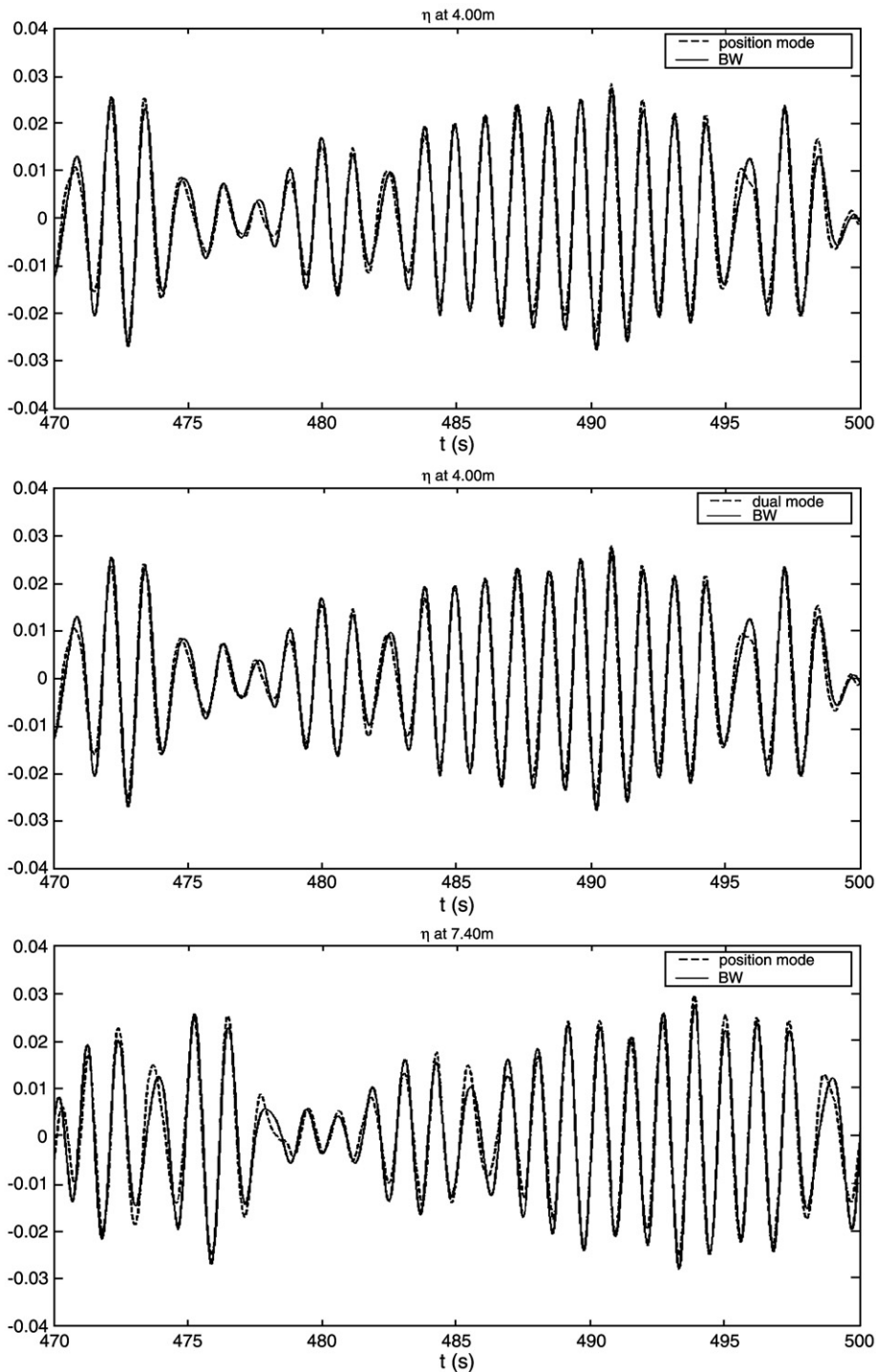


Fig. 7. The surface elevation measured at 4.0 m and 7.4 m in *position mode* and *dual mode*, respectively, compared with the numerical calculation (BW) choosing  $x_0=96$  m.

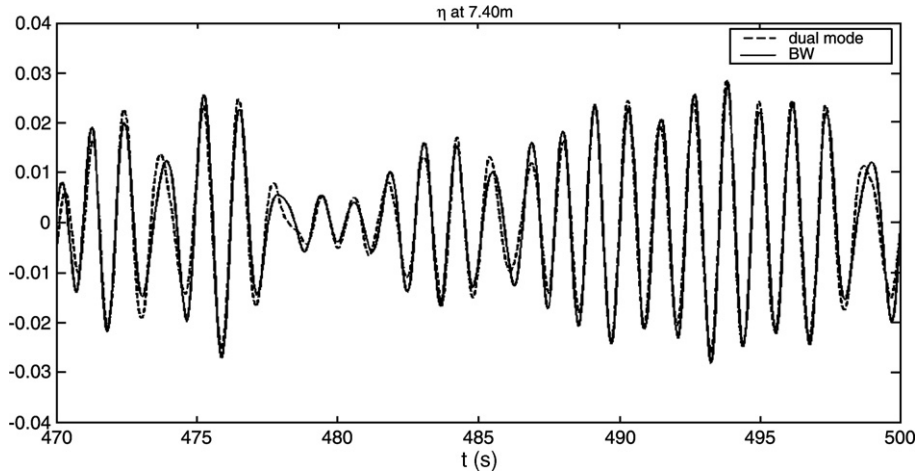


Fig. 7 (continued).

where the evanescent modes are given in a complex representation (Schäffer and Steenberg, 2003):

$$\Gamma \equiv i \sum_{j=1}^{\infty} e_j \quad (14)$$

The transfer function  $e_j$  is defined as

$$e_j = \frac{k_j}{k_{xj}} c_j = \frac{1}{\cos \alpha_j} c_j \quad (15)$$

Here  $\vec{k}_j = (k_{xj}, k_{yj})$  is the complex wave number vector,  $k_j \equiv |\vec{k}_j|$  denotes the length of the wave number vector,  $c_j$  is

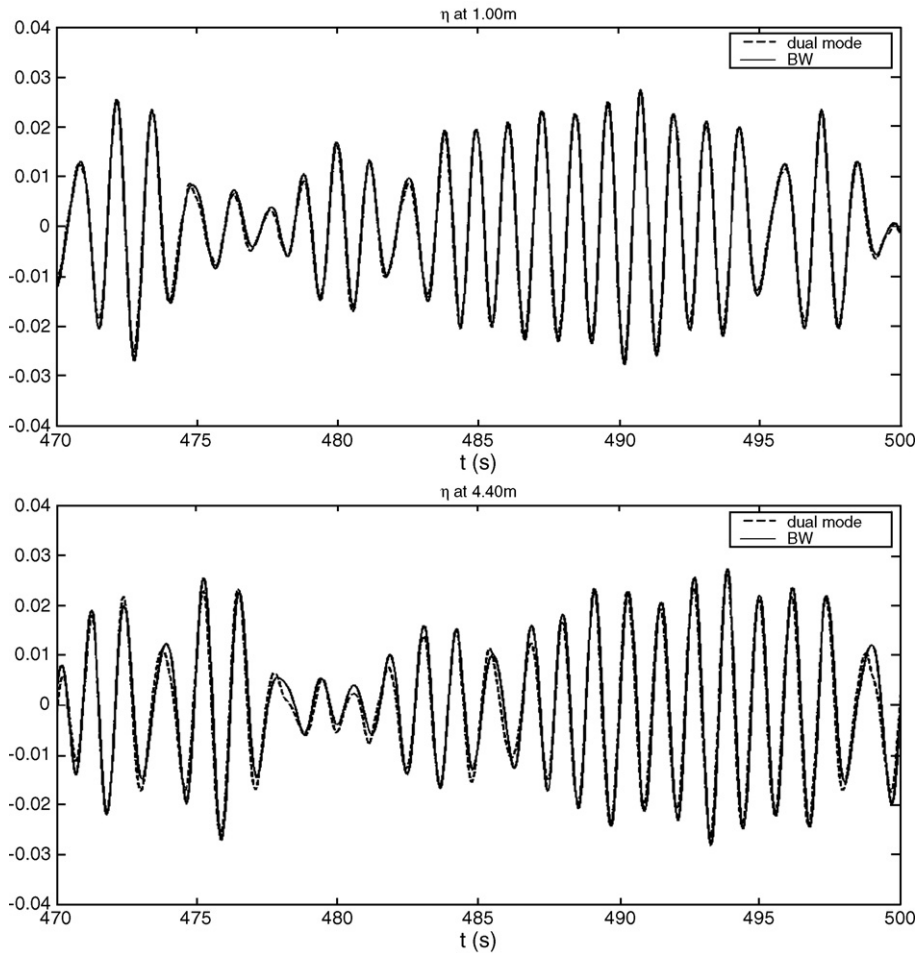


Fig. 8. The surface elevation measured at 1.0 m and 4.4 m in *dual mode* compared with the numerical calculation (BW) choosing  $x_0=99$  m. Altogether this gives an identical target (BW) to Fig. 7.

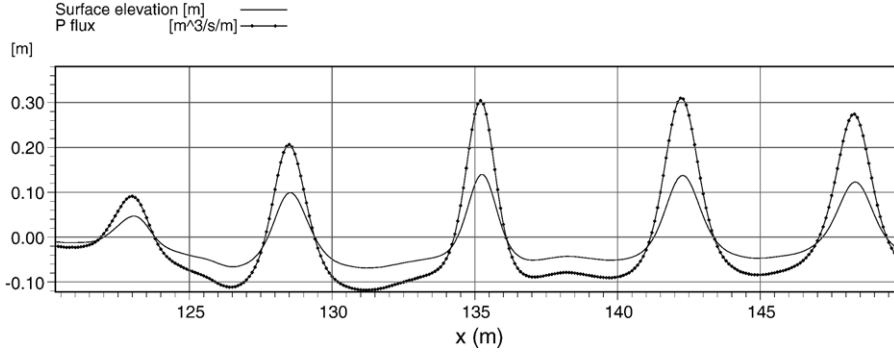


Fig. 9. Profiles of  $P$  flux and surface elevation at constant water depth  $h=0.4$  m at  $t=180$  s.

the transfer function for normally emitted waves ( $k_y=0$ ) given by

$$c_j = \frac{4\sinh^2 k_j h}{2k_j h + \sinh 2k_j h} \quad (16)$$

and

$$k_y = k \sin \alpha = k_j \sin \alpha_j \quad (17)$$

$$\cos \alpha_j = \frac{k_{xj}}{k_j} = \sqrt{1 - \frac{k^2 \sin^2 \alpha}{k_j^2}} = \sqrt{1 + \frac{k^2 \sin^2 \alpha}{|k_j|^2}} \geq 1 \text{ for } j \geq 1 \quad (18)$$

Here  $k_j$  is purely imaginary and satisfies the linear dispersion relation generalized to complex wave numbers corresponding to evanescent modes:

$$\omega^2 = g k_j \tanh k_j h \quad (19)$$

Fig. 3 shows the 2D transfer function  $\Gamma$  with respect to non-dimensional wave number and frequency ( $k_y h, \omega \sqrt{h/g}$ ). Fig. 3 includes cases of  $|k_y| \leq k$  (serpent wavelength longer than or equal to length of progressive wave), and also  $|k_y| > k$  (serpent wavelength shorter than progressive wave). The curve on the surface in the graph shows the critical value  $|k_y| = k$ . Progressive waves,  $|k_y| \leq k$  correspond to the lower right side of the critical curve.

The transfer function  $\Gamma$  is modified to  $\Gamma_m$  by damping at high frequencies on  $k_y$  and  $\omega$  as done for  $\Lambda$ , see Fig. 4. Fig. 5 shows  $\Gamma$  and  $\Gamma_m$  for normally emitted waves ( $k_y=0$ ) in a wave flume.

The surface elevation at the moving paddle in physical space is expressed as

$$\eta_{I,0}(y, t) = \eta_I(y, t) + F_{2D}^{-1} \{ \Gamma_m(k_y, \omega) F_{2D} \{ X(y, t) \} \} \quad (20)$$

where  $F_{2D}$  represents the 2D Fourier transform.

### 2.2. Non-linear shallow water wave generation

For non-linear shallow water waves with small dispersion such as Cnoidal waves, the horizontal particle velocity is almost uniform over depth. A Cnoidal wavemaker theory for wave flumes has been developed by Goring (1979). Based on this theory, the time-domain relation between the depth-averaged velocity from the numerical model and the paddle position is then given for 3D wave basins, as

$$\frac{\partial X^{sw}(y, t)}{\partial t} + \frac{\partial X^{sw}(y, t)}{\partial y} V(X^{sw}(y, t), y, t) = U(X^{sw}(y, t), y, t) \quad (21)$$

subjected to relevant initial and boundary conditions. Here  $V$  is the depth-averaged horizontal particle velocity in the  $y$  direction. This captures the non-linearity of the numerical model, but corresponds to the shallow water limit for the wave generation.

For active absorption with dual control, the associated surface elevation at the moving paddle is also needed:

$$\eta_{I,0}(y, t) = \eta(X^{sw}(y, t), y, t) \quad (22)$$

### 2.3. Ad hoc unified 3D wave generation

We now combine the linear fully dispersive wavemaker theory and the method of non-linear long wave generation for 3D wave basins. We compute the shallow water paddle position from Eq. (21) taking the  $(U, V)$  field from the numerical wave propagation model, and then compensate for the disregarded

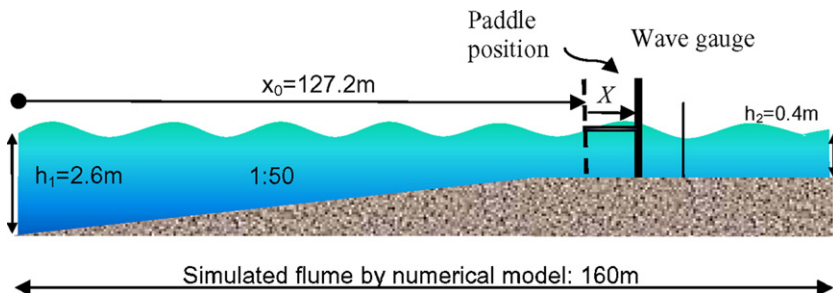


Fig. 10. Sketch of the combined model.

dispersion using Eq. (12). For vanishing dispersion this procedure reduces to non-linear long wave generation, while fully dispersive linear wavemaker theory recovers in case of vanishing non-linearity.

In order to avoid slow drift of the paddle which is due to tiny deviation from the exact signals and the numerical integration, we add a small term proportional to the paddle signal to the differential equation for the effect of a first order high-pass filter

(Humpherys, 1970). Let  $\omega_c$  denote the characteristic angular frequency of this filter, then the unified wave generation is altogether governed by

$$\begin{aligned} \frac{\partial X^{sw}(y,t)}{\partial t} + \frac{\partial X^{sw}(y,t)}{\partial y} V(X^{sw}(y,t),y,t) + \omega_c X^{sw}(y,t) \\ = U(X^{sw}(y,t),y,t) \end{aligned} \quad (23)$$

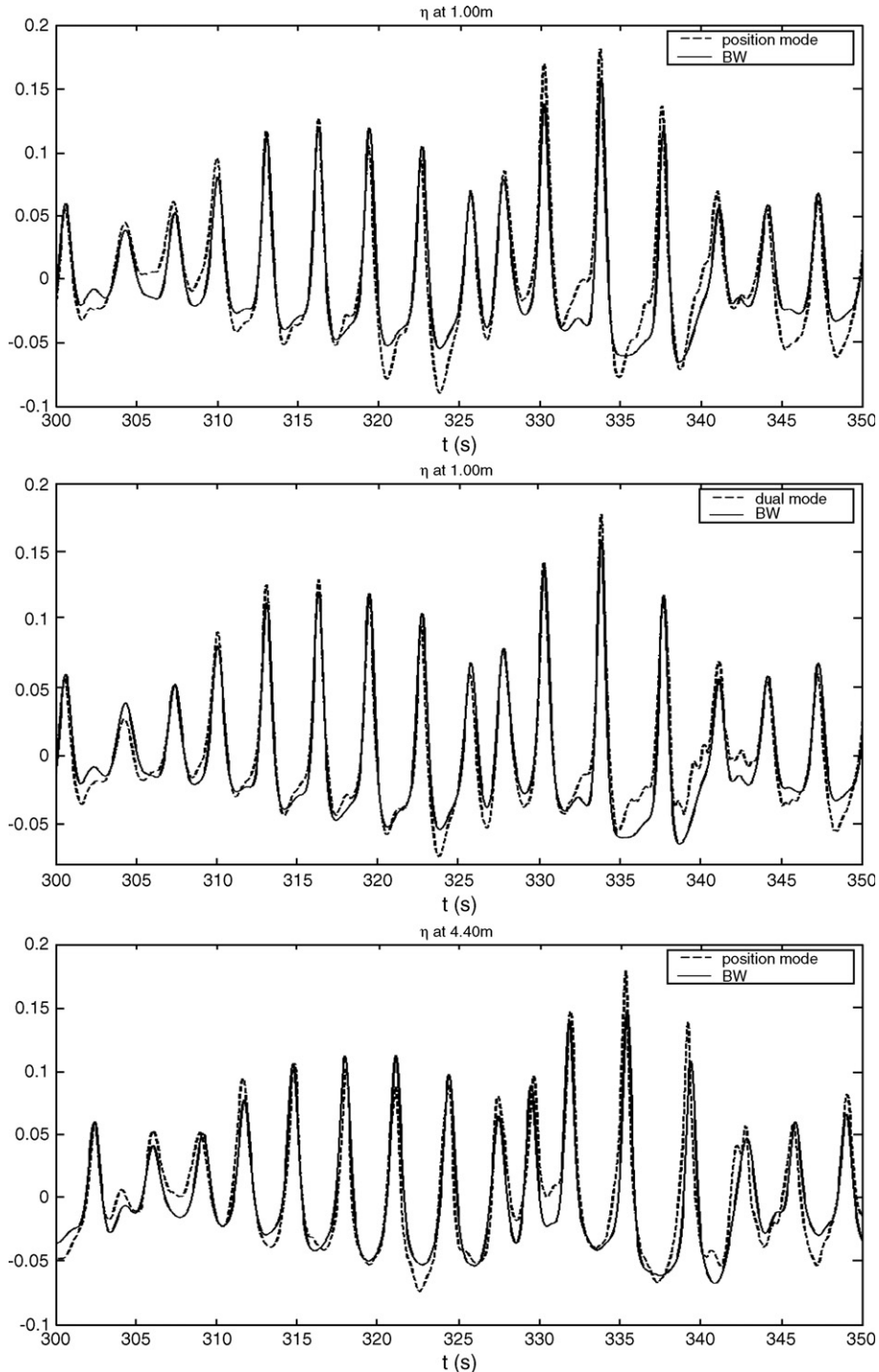


Fig. 11. The surface elevation measured at 1.0 m and 4.4 m in *position mode* and *dual mode*, respectively, compared with the numerical calculation (BW).

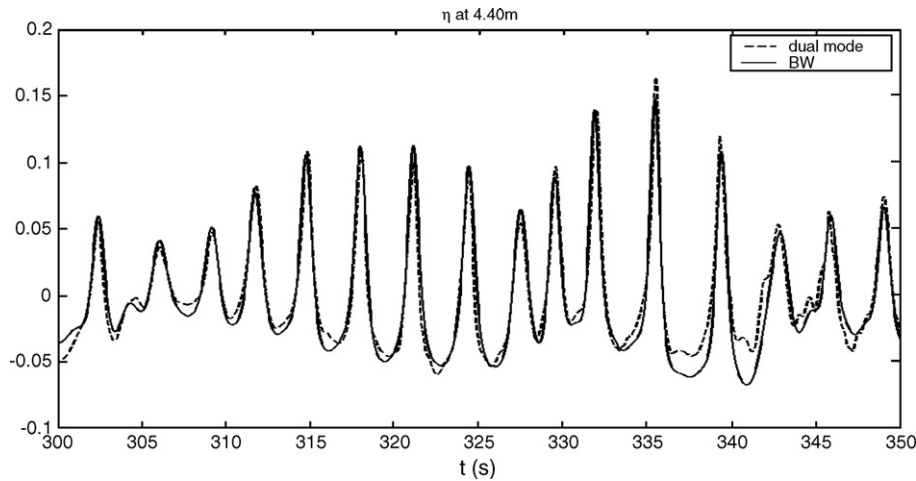


Fig. 11 (continued).

followed by the dispersion correction

$$X(y, t) = F^{-1}\{A_m(\omega)F\{X^{sw}(t)\}\} \quad (24)$$

For dual control active absorption, the expected surface elevation at the moving paddle is needed. Without the evanescent-mode correction, we have

$$\eta_{l,0}^p(y, t) = \eta(X(y, t), y, t) \quad (25)$$

where the superscript ‘p’ on the quantity  $\eta_{l,0}^p(y, t)$  indicates that only progressive waves are accounted for. Here, on the right-hand side,  $\eta(x, y, t)$  is the field from the numerical wave propagation model.

With the evanescent-mode correction, the surface elevation at the moving paddle is

$$\eta_{l,0}(y, t) = \eta_{l,0}^p(y, t) + \eta_0^{eva} \quad (a) \quad (26)$$

$$\eta_0^{eva} = F_{2D}^{-1}\{\Gamma_m(k_y, \omega)F_{2D}\{X(y, t)\}\} \quad (b)$$

where  $\eta_0^{eva}$  is the correction part for the evanescent modes.

### 3. Experimental validation in wave flumes

Physical tests are made in a 0.75 m wide, 1.20 m deep, and 23 m long flume. The flume is equipped with a piston-type wavemaker with an electric drive system including a brushless AC motor and an integrated linear drive/bearing system at one end ( $x=0$ ), and an efficient passive absorber at the other end. The wavemaker is controlled by DHI AWACS with two control modes for consistent non-linear wave generation. In all tests the numerical model is run beyond the wavemaker to provide a reference for the wave elevation time series measured in the physical experiment.

#### 3.1. Irregular waves propagating on constant water depth

With the purpose of testing the dispersion correction and the evanescent-mode correction, we make a test on a rather deep water case for irregular waves. The simulated wave flume is 160 m long with a constant water depth of  $h=0.7$  m. The irregular incoming wave conditions are synthesized from a

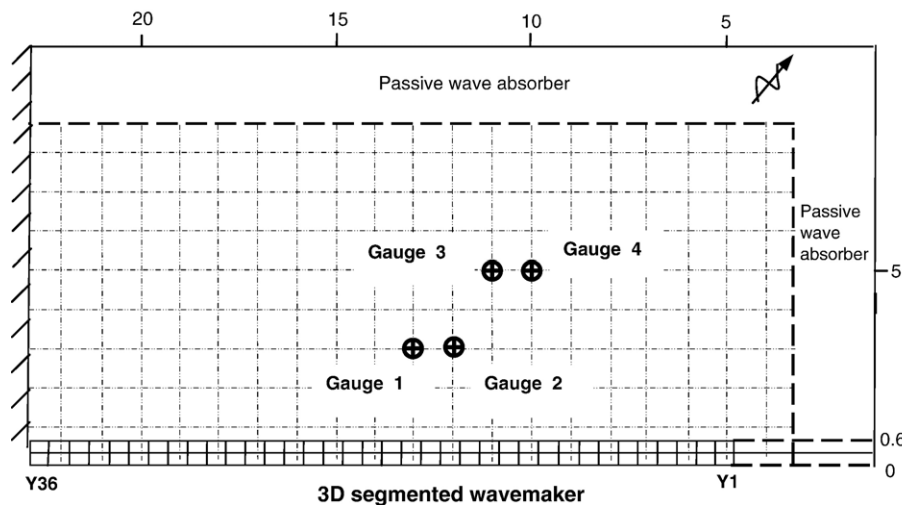


Fig. 12. Sketch of the test set-up. Note: the basin coordinate here is specially for the facility and physical tests.

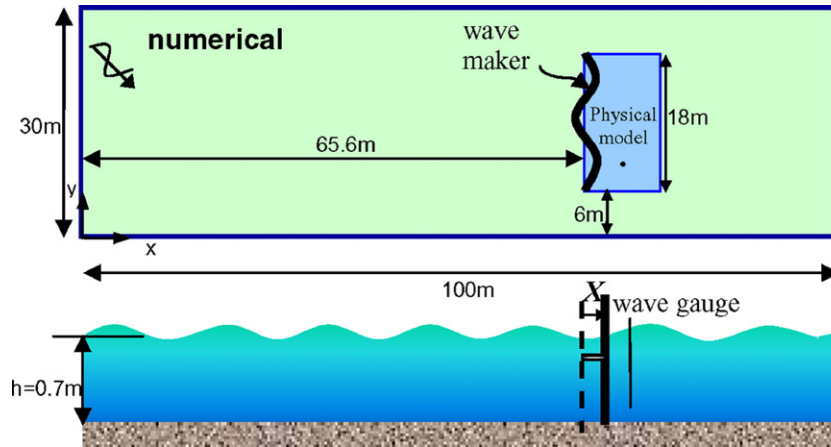


Fig. 13. Sketch of plan view and vertical cross-section of the combined model.

standard JONSWAP frequency spectrum, with a significant wave height of  $H_{m0}=0.05\text{ m}$ , a peak period of  $T_p=1.2\text{ s}$ , and the relevant shape parameters,  $\gamma=3.3$ ,  $\sigma_a=0.07$ ,  $\sigma_b=0.09$ . The spectrum is truncated omitting periods smaller than 0.95 s. This gives a range of  $kh$  between 2.02 and 3.13. The truncated spectrum is rescaled in the numerical model to retain the specified  $H_{m0}=0.05\text{ m}$ . The time step is taken as  $dt=0.01\text{ s}$  and the grid spacing is  $dx=0.1\text{ m}$ . We set fixed wave gauges at  $x=100\text{ m}$  and  $x=103.4\text{ m}$  where  $x=0$  coincides with the up-wave boundary of the numerical model. For the data transfer between the numerical and physical models, we choose to test two different locations,  $x_0=96\text{ m}$  and  $x_0=99\text{ m}$ , where  $x_0$  is the mean paddle position for the physical flume. See Fig. 6 for the sketch of the combined model.

The surface elevations measured at 4.0 m (gauge 1) and 7.4 m (gauge 2) from the mean paddle position in the physical flume in *position mode* and *dual mode*, respectively, are compared with the numerical calculations when choosing  $x_0=96\text{ m}$  in Fig. 7. The measurements match numerical calculations reasonably well in each mode at each gauge. The correlation coefficients between measured and numerical surface elevations are 0.98 at gauge 1 and 0.96 at gauge 2 for the entire 10-min period of the physical test in *position mode*. In *dual mode*, they are 0.99 at gauge 1 and 0.97 at gauge 2 for the entire 10-min

period of the physical test. *Dual mode* reproduces waves in flume with the same quality as *position mode*. But the big advantage of *dual mode* is simultaneous wave generation and active absorption, although in the present tests, the active absorption is not needed.

The comparison of the surface elevations measured at 1.0 m (gauge 1) and 4.4 m (gauge 2) from the mean paddle in the physical flume in *dual mode* with the numerical calculations are shown in Fig. 8 for the case of  $x_0=99\text{ m}$ . Note that the gauge positions were chosen to leave the distance to the up-wave boundary of the numerical model unchanged. Thus the target (BW) in the two first panels of Fig. 7 is identical with the target of the first panel in Fig. 8. The same is true for the last two panels of Fig. 7 and the last panel of Fig. 8. The correlation coefficients between measured and numerical surface elevation are 0.99 at gauge 1 and 0.98 at gauge 2 for the 10-min duration of physical test in *dual mode* as well as in *position mode*. All the measurements in the physical flume match the numerical calculation quite well. The measurement matches the numerical result better when the wave gauge is closer to the mean paddle position. This is probably mainly due to the inaccuracies of the numerical model. However, the combined model is almost independent of the paddle's mean location. Therefore, the combined model is not very

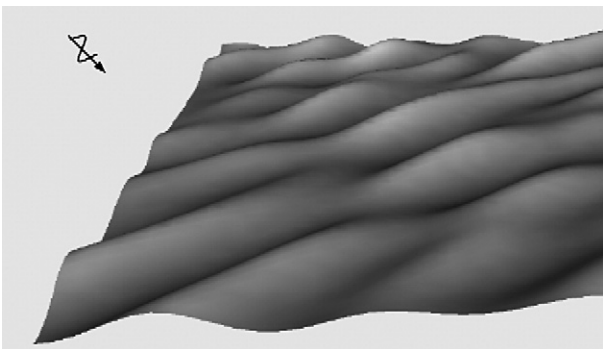


Fig. 14. Snapshot of numerical surface elevation in the physical model's area at  $t=44\text{ s}$ .

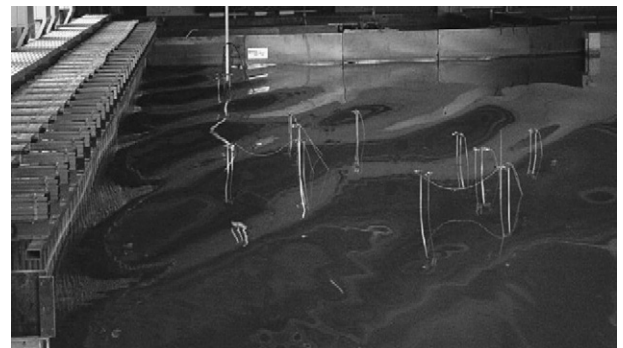


Fig. 15. Snapshot of wave filed in the physical basin.

sensitive to where the physical model takes over from the numerical model.

### 3.2. Irregular waves propagating up a slope

Another example considers irregular waves propagating up a slope from a deep plateau to a shallow plateau. At the end of the slope the non-linearity is very high. The length of the simulated wave flume is 160 m. The internal waves in the numerical model are generated at a water depth of  $h=2.6$  m. The bed slope is 1:50 up to a water depth of  $h=0.4$  m. The irregular incident wave conditions were synthesized from a standard JONSWAP frequency spectrum, with a significant wave height of  $H_{m0}=0.12$  m, a peak period of  $T_p=3$  s, and the relevant shape parameters,  $\gamma=3.3$ ,  $\sigma_a=0.07$ ,  $\sigma_b=0.09$ . The spectrum is truncated omitting periods smaller than 2.6 s. The time step is taken as  $dt=0.01$  s and the grid spacing is  $dx=0.1$  m. As an example Fig. 9 shows profiles of the volume flux defined as the depth-integrated horizontal velocity ( $P$  flux) and surface elevation at  $t=180$  s, extracted from the numerical output at the part of the flume with constant water depth of  $h=0.4$  m. After shoaling, waves turn to irregular non-linear long waves.

The physical model is set at flat water depth of  $h=0.4$  m. We set two fixed wave gauges at  $x=128.2$  m (gauge 1) and

$x=131.6$  m (gauge 2) in the whole simulated flume. Since the combined model is not very sensitive to the location of mean paddle position for data transfer from numerical model to physical model,  $x_0=127.2$  m is chosen arbitrarily as the mean paddle position for physical flume test. See Fig. 10 for the sketch of the combined model.

The surface elevations measured at 1.0 m and 4.4 m from the mean paddle in the physical flume in *position mode* and *dual mode*, respectively, are shown in Fig. 11, compared with the numerical calculations. The correlation coefficients are 0.92 at both gauge 1 and gauge 2 for the entire 10-min duration in *position mode*. They are 0.94 at gauge 1 and 0.95 at gauge 2 for the entire duration in *dual mode*. Although deviations occur especially for the higher waves the match is quite good considering the very high non-linearity of the waves. The Ursell number is about 71 at the significant wave height and peak period, and thus about twice that for the highest waves in the wave train. In fact, some wave breaking occurred in the physical flume on the down-wave side of the wave gauges. Wave breaking was not accounted for in the numerical model. The dominant errors are due to the limitation of Boussinesq equations rather than the ad hoc unified wave generation. This conclusion is based on the ability of the ad hoc unified wave generation theory to

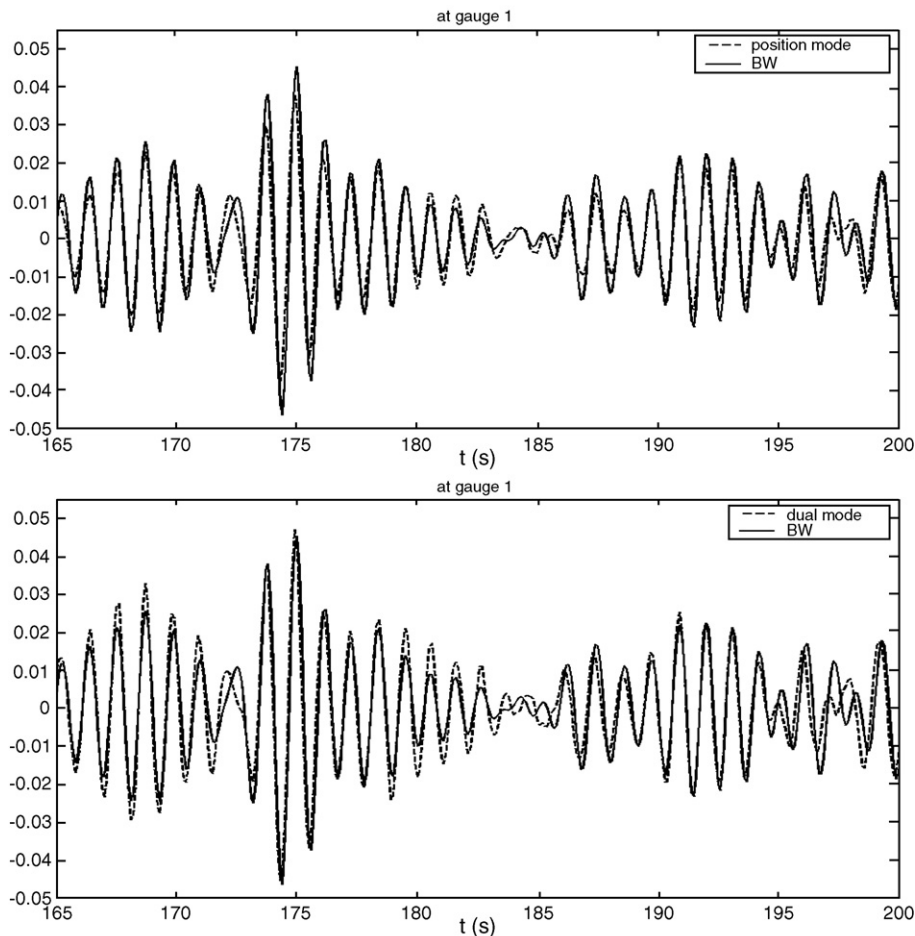


Fig. 16. The surface elevation measured at gauge 1 compared with the numerical calculation (BW).

produce accurate highly nonlinear regular waves in the flume when substituting the numerical model with Stream Function wave theory (See Zhang and Schäffer, in press, and the comments in the introduction). For this non-linear wave case, *dual mode* gives better results than *position mode*. The reason for this is probably that in *dual mode*  $\eta_{1,0}$  is provided and the control system thus gets a second chance for making slight corrections to paddle signal in case the measured surface elevation does not exactly match the expected one.

Altogether, the deterministic combination of numerical and physical wave flume models using the ad hoc unified wave generation for passing waves from a numerical model to a physical wave flume appears to be appropriate.

#### 4. Experimental validation in wave basins

The tests are made in a wave basin with a segmented 3D wavemaker at DHI. The 36-segment 3D wavemaker is of

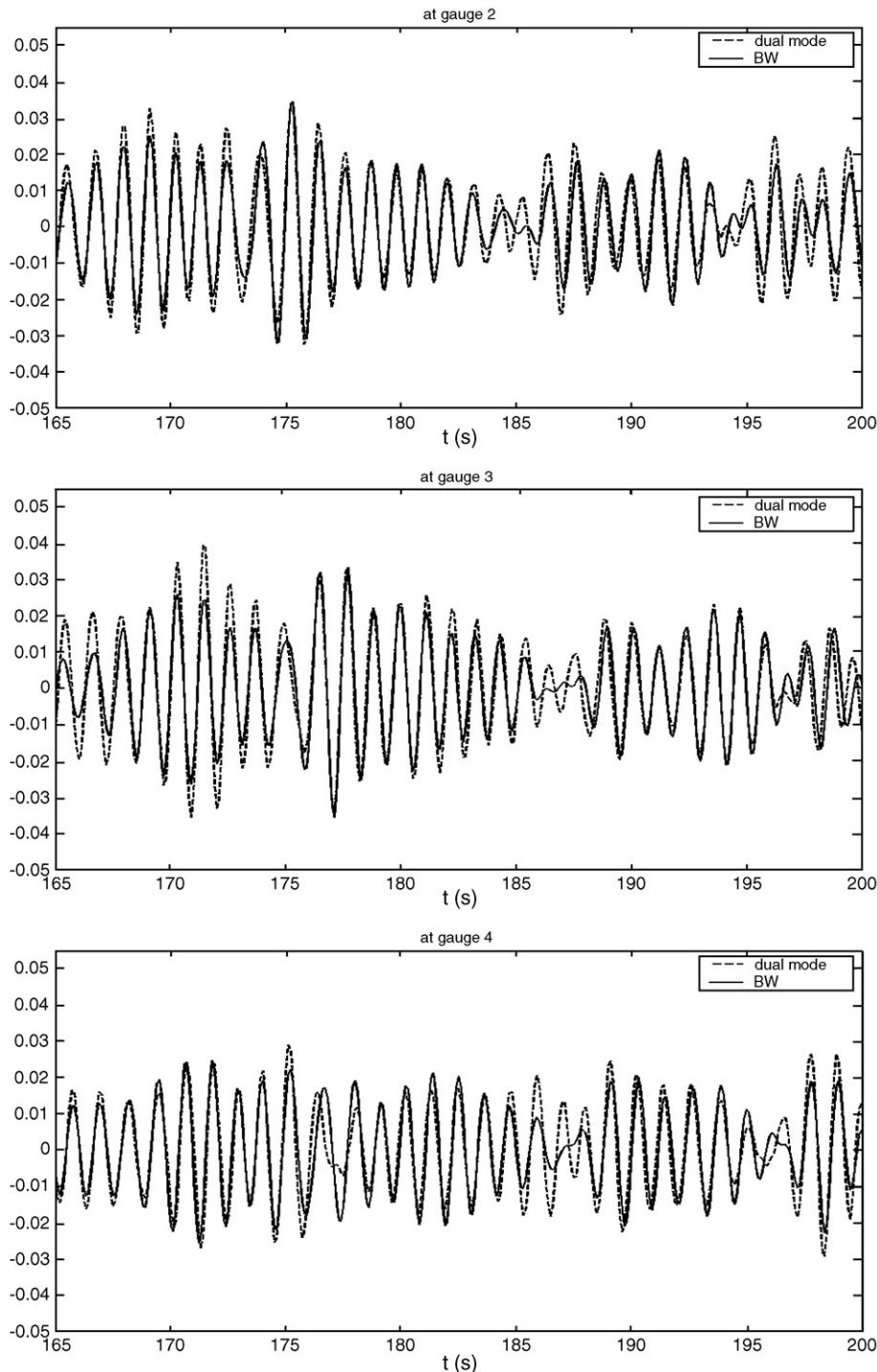


Fig. 17. The surface elevations measured at gauge 2–4 compared with the numerical calculation (BW).

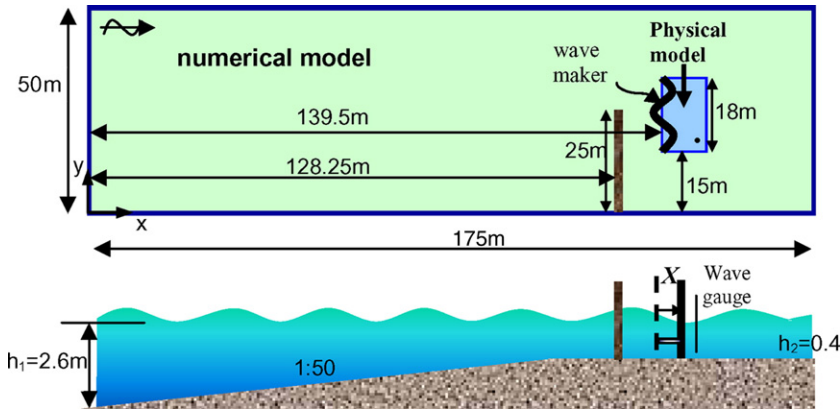


Fig. 18. Sketch of plan view and vertical cross-section of the combined model.

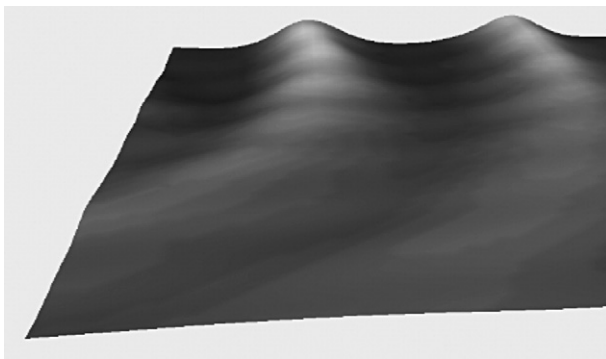


Fig. 19. Snapshot of numerical surface elevation in the physical model's area at  $t=205$  s.

encoder feedback. The 3D wavemaker is controlled by the DHI 3D AWACS with two control modes, *dual mode* and *position mode*, for non-linear wave generation with and without active absorption. The section available for the present tests is about 8.5 m long in the  $x$  direction, and 19.5 m wide in the  $y$  direction. At the down-wave boundaries of the basin, some passive wave absorbers are installed. The up-wave boundary along the  $x$  direction is made up by a guide-wall. The experimental set-up is sketched in Fig. 12, which also shows the location of the wave gauges for the first set of tests.

#### 4.1. Directional irregular waves propagating on constant water depth

This example considers a rather deep water case for directional irregular waves based on the irregular deep water wave case in the flume. The simulated wave basin is 100 m long ( $x$  direction) and 30 m wide ( $y$  direction) with a constant water depth of  $h=0.7$  m. The irregular incoming wave conditions are synthesized from a standard JONSWAP frequency spectrum,

piston-type with vertical hinges between the segments providing a linear segmentation of the paddle front. The paddle width is  $dy=0.5$  m with 1.2 m height and the maximum stroke is 0.6 m. Precision control of each actuator is achieved using a brushless AC servomotor with a ball screw transmission and

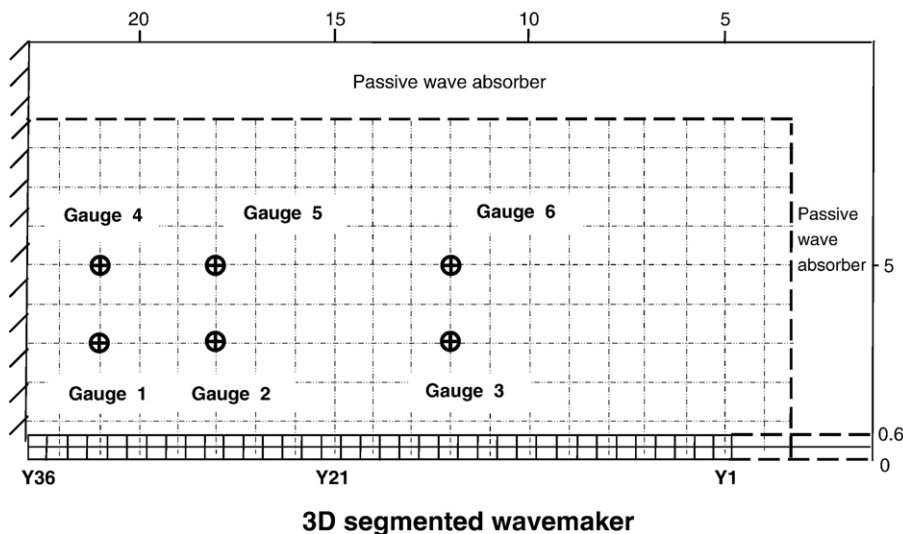


Fig. 20. Sketch of the basin test set-up.



Fig. 21. Snapshot of wave field in the physical basin.

with a significant wave height of  $H_{m0}=0.05$  m, a peak period of  $T_p=1.2$  s, and the relevant shape parameter,  $\gamma=3.3$ ,  $\sigma_a=0.07$ ,  $\sigma_b=0.09$ . The spectrum is truncated omitting periods smaller than 0.95 s. The truncated spectrum is rescaled in the numerical model to retain the specified  $H_{m0}=0.05$  m. The mean wave direction is  $-30^\circ$ . The maximum deviation from the mean wave direction is chosen as  $30^\circ$ . The directional distribution is expressed as  $\cos^4(\alpha+30^\circ)$ . The 18 m-long wavemaker in the physical wave basin is arbitrarily placed from  $y=6$  m to 24 m at  $x_0=65.6$  m, where  $x=0$  coincides with the up-wave boundary of

the numerical model. Thus,  $x_0=65.6$  m is the mean paddle position for the data transfer from numerical to physical model, see Fig. 13 for a sketch of the combined model. The paddle ‘Y36’ near the guide wall in Fig. 12 corresponds to  $y=24$  m, and ‘Y1’ corresponds to  $y=6$  m.

Fig. 14 shows a snapshot of the surface elevation extracted from the numerical calculation in the physical model’s area at  $t=44$  s. The left boundary coincides with the physical wavemaker.

Physical tests are made in *dual mode* and *position mode*, respectively. Time series of surface elevation at four wave gauges are measured in the wave basin. The locations of wave gauges have been shown in Fig. 12. A snapshot of the wave field in the physical basin is shown in Fig. 15, which is comparable to Fig. 14. The calm area in the upper right of the physical field does reduce the equivalence with the numerical model. This is due to the guide wall and the associated lee zone and diffraction.

The time series of surface elevation measured at gauge 1 are compared with the numerical calculations in Fig. 16 using *position mode* and *dual mode*, respectively. The match is quite good although deviations occur. *Position mode* gives smaller waves than *dual mode*. Using *dual mode* the measurements at the other three gauges are compared with numerical calculations in Fig. 17. In *dual mode*, the correlation coefficients are 0.89–0.90 at all four gauges for the entire 10-min

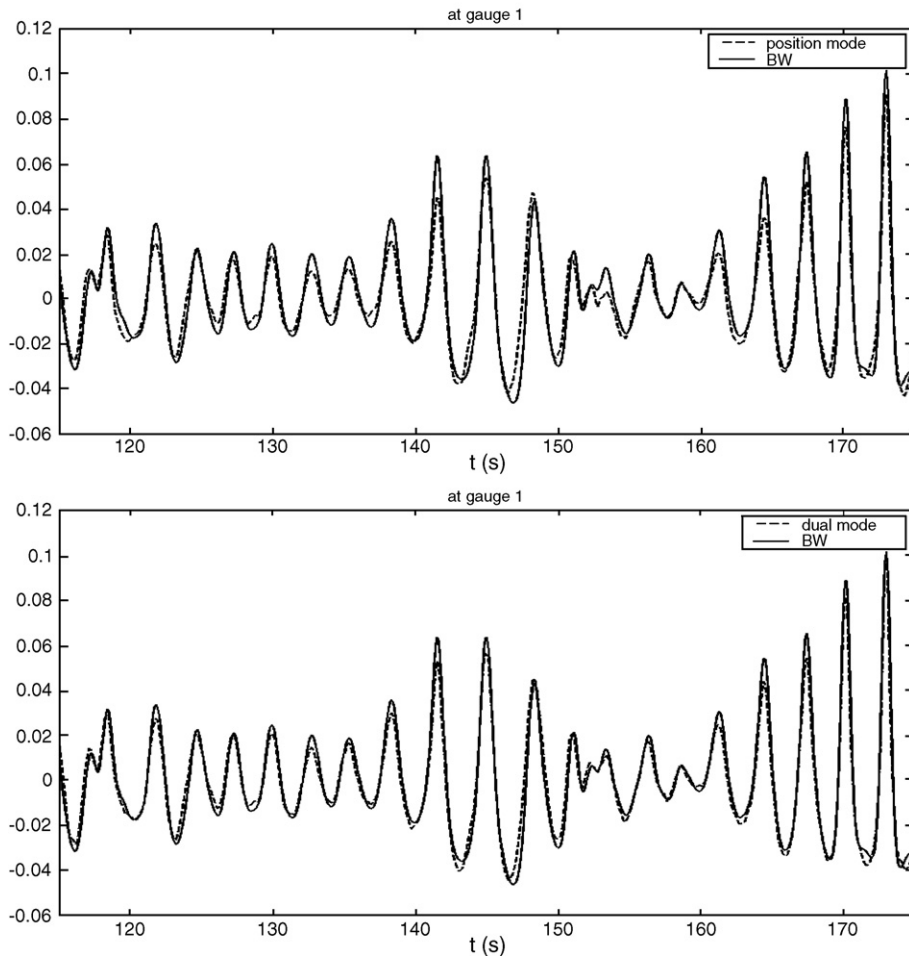


Fig. 22. The surface elevation measured at gauge 1 compared with the numerical calculation (BW).

period of the physical test. In *position mode*, the coefficients are 0.90–0.91.

#### 4.2. Irregular waves behind a breakwater after propagating up a slope

To test directional non-linear shallow water waves, the last example considers irregular waves propagating up a slope from a

deep plateau to a shallow plateau with a breakwater, based on the flume case in Section 3.2. See the sketch of the combined model in Fig. 18. The simulated numerical wave basin is 175 m long (in  $x$  direction), 50 m wide (in  $y$  direction). The internal waves in the numerical model are generated at a water depth of 2.6 m. The bed slope is 1:50 up to a water depth of 0.4 m. The breakwater is set on the shallow plateau, from  $x=128.25$  m to  $x=128.75$  m,  $y=0$  to  $y=25$  m. The irregular incoming wave conditions are

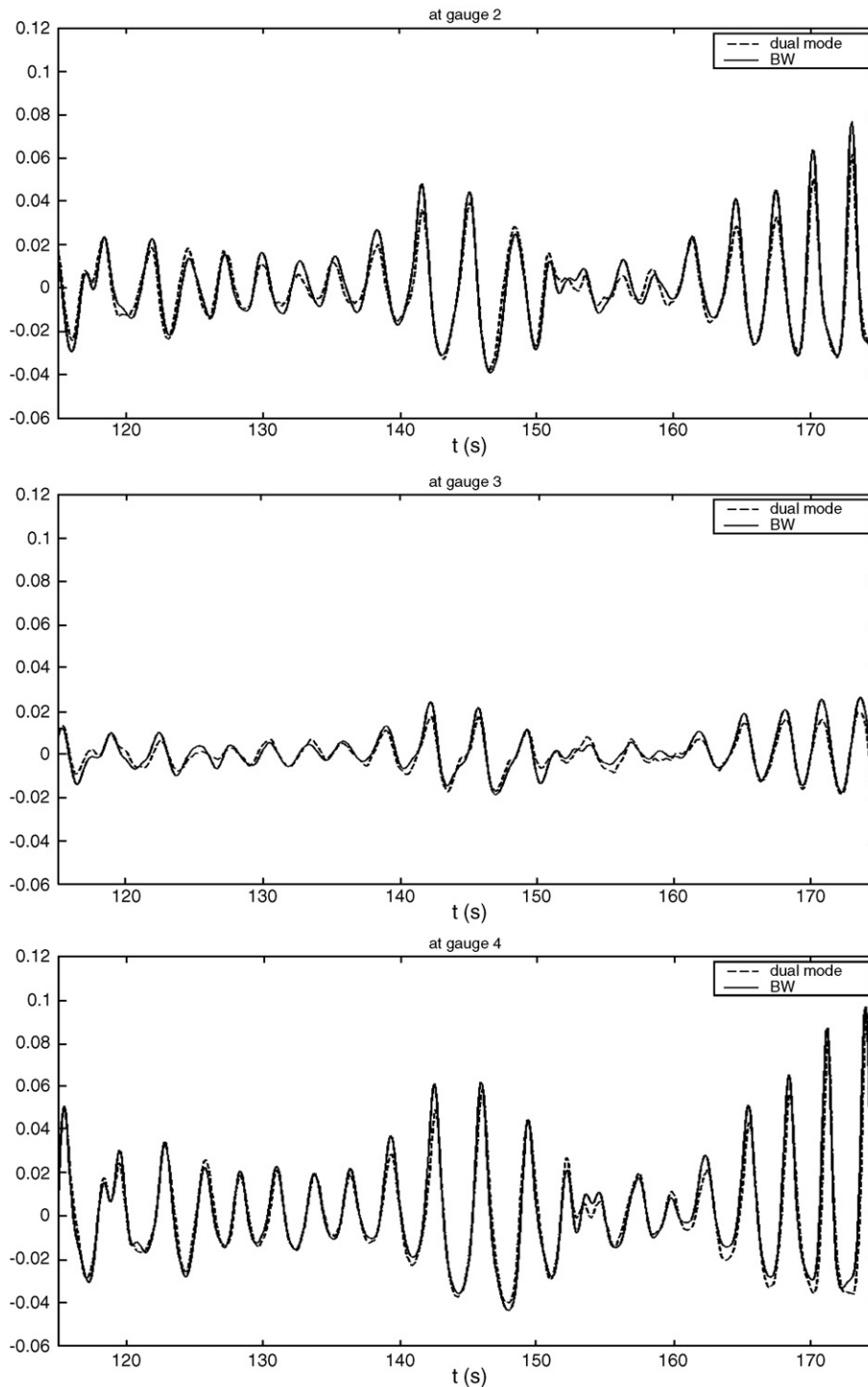


Fig. 23. The surface elevation measured at gauge 2–6 compared with the numerical calculation (BW).

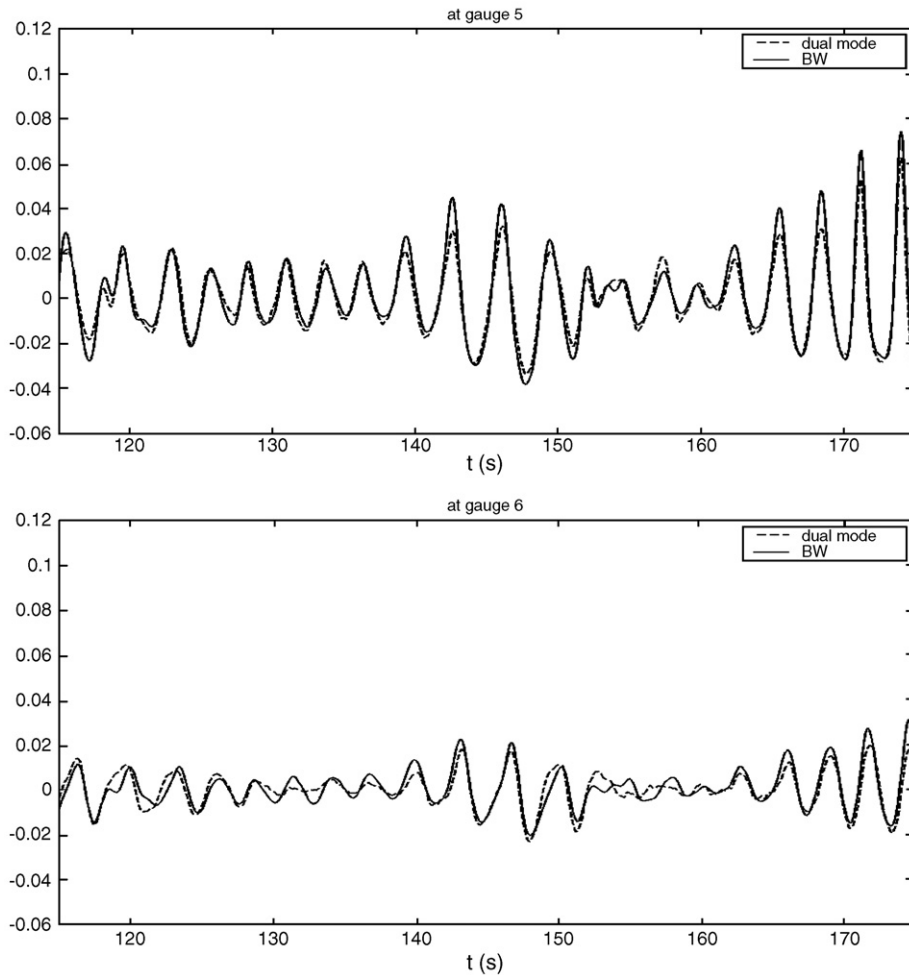


Fig. 23 (continued).

synthesized from a standard JONSWAP frequency spectrum, with a significant wave height of  $H_{m0}=0.09$  m, a peak period of  $T_p=3$  s, and the relevant sharp parameter,  $\gamma=3.3$ ,  $\sigma_a=0.07$ ,  $\sigma_b=0.09$ . The incoming waves propagate along the  $x$  direction. The spectrum is truncated omitting periods smaller than 2.6 s. The truncated spectrum is rescaled in the numerical model to retain the specified significant wave height. Based on the non-linear irregular case in the flume, we know that at the end of the slope waves are irregular non-linear long waves. Then waves turn to irregular non-linear long waves with slight directional spreading behind the breakwater due to slightly different diffraction of each spectral component. Fig. 19 shows a snapshot of the numerical calculation in the physical model's area at  $t=205$  s. The shape of non-linear long wave is shown clearly on the upper side. On the lower side, the surface is almost still due to the breakwater.

The 18 m-long wavemaker in the physical wave basin is set from  $y=15$  m to 33 m and  $x=139.5$  m in the whole unified model. Thus  $x_0=139.5$  m is the location of the mean paddle position for the data transfer from the numerical to the physical model. In the physical model, the set-up of tests are identical to the one used before except for the location of wave gauges, see Fig. 20. The paddle 'Y36' corresponds to  $y=33$  m in the combined model, and 'Y21' corresponds to  $y=25$  m which is

parallel to the end of the breakwater. Fig. 21 shows a snapshot of the wave field in the physical basin which resembles the numerical snapshot in Fig. 19.

The time series of surface elevation measured at gauge 1 in *position mode* and *dual mode* are compared with the numerical calculation in Fig. 22. The measurements match the numerical calculation well in both modes but with slightly lower peaks in the physical model. *Dual mode* gives a little better results. The measurements at other gauges in *dual mode* are compared with numerical calculations in Fig. 23. As expected, the wave amplitudes decrease gradually from gauge 1 to 3 and from gauge 4 to 6 as  $y$  decreases. This is due to the wave diffraction, which also introduces small phase changes among the signals at gauges 4–6 and 1–3, respectively.

In *dual mode*, the correlation coefficients are 0.98, 0.96, 0.94, 0.98, 0.97, and 0.91 for gauges 1–6, respectively, in the whole 4-min period of the physical test. In *position mode*, the respective coefficients are 0.97, 0.94, 0.92, 0.97, 0.96 and 0.86. All the measurements in the physical basin match the numerical calculation quite well. *Dual mode* gives a little larger correlation coefficients at each gauge than *position mode* for this case. The measurements are closer to the numerical results when the wave gauges are closer to the guide wall where the wave amplitudes are relatively high in the wave field.

## 5. Summary and conclusions

In this paper, a deterministic combination of numerical and physical coastal wave models has been presented. A Boussinesq model MIKE 21 BW was chosen for numerical calculations. Piston-type 2D/3D wavemakers and the associated active absorption control system provide the interface between the numerical and physical models. An ad hoc unified 3D wave generation theory has been devised for providing the link between the numerical and physical models. This wave generation theory accounts for shallow water non-linearity and compensates for local wave phenomena (evanescent modes) near the wavemaker. The data transfer between the two models is on a deterministic level with detailed wave information transmitted along the wavemaker.

The practical examples indicate that the ad hoc unified wave generation theory is adequate for successfully passing 2D and 3D coastal waves from a numerical model to a physical model. The combined model is not very sensitive to where the physical model takes over from the numerical model.

In conclusion, the deterministic combination of numerical and physical coastal wave models is feasible either with or without active absorption. This method is particularly suitable for non-linear directional long waves. This conclusion was supported by the experimental results.

## Acknowledgments

This work is funded by the Danish Technical Research Council (STVF contract no. 26-01-0043).

## References

- Dean, R.G., Dalrymple, R.A., 1984. Wavemaker theory. *Water Wave Mechanics for Engineers and Scientists*, pp. 170–185.
- Gierlefsen, T., Vargas, B.M., Pires, V.P.L., Acetta, D., 2003. Numerical and physical modelling of storm waves at Rio de Janeiro yacht club. COPEDEC Colombo, Sri Lanka, 15–19 Sept. 2003.
- Goring, D.G., 1979. Tsunamis—the propagation of long waves onto a shelf. Doctoral Dissertation, Report. W.M. Keck laboratory of hydraulics and water resources. California, pp. 9–45.
- Humpherys, D.S., 1970. *The Analysis, Design, and Synthesis of Electrical Filters*. Prentice-Hall, Englewood Cliffs, N.J., pp. 1–87.
- Kamphuis, J.W., 1995. Composite modelling — an old tool in a new context. *Proc. 26th Congress of International Association of Hydraulic Research, (IAHR)*, London, vol. 2, pp. 230–235.
- Kamphuis, J.W., 1996. Physical modelling of coastal processes. In: Liu, P. (Ed.), *Advances in Coastal and Ocean Engineering*, vol. 2. World Scientific Publishing, Singapore, pp. 79–114.
- Kamphuis, J.W., 2000. Designing with Models. *Proceedings of the 27th International Conference on Coastal Engineering*, Sydney, July, 2000, pp. 19–32.
- Kofoed-Hansen, H., Sloth, P., Sørensen, O.R., Fuchs, J., 2000. Combined numerical and physical modelling of seiching in exposed new marina. *Proceedings of the 27th International Conference on Coastal Engineering*, Sydney, July, 2000.
- Madsen, O.S., 1974. A three-dimensional wavemaker, its theory and application. *Journal of Hydraulic Research* 12.
- Madsen, P.A., Sørensen, O.R., 1992. A new form of the Boussinesq equations with improved linear dispersion characteristics. Part 2. A slowly-varying bathymetry. *Coastal Engineering* 18, 183–204.
- Oumeraci, H., 1999. Strengths and limitations of physical Modelling in coastal Engineering – synergy effect with numerical modelling and field measurement. *Proceedings of HYDRALAB-Workshop in Hannover, Germany, Feb. 1999*, pp. 7–38.
- Schäffer, H.A., 1999. On hybrid modelling in coastal and ocean engineering. *Proceedings of HYDRALAB-Workshop in Hannover, Germany, Feb., 1999*.
- Schäffer, H.A., 2001. Active wave absorption flumes and 3D basins. *Proceedings of Waves 2001, San Francisco, California, Sept., 2001*.
- Schäffer, H.A., Jakobsen, K.P., 2003. Non-linear wave generation and active absorption in wave flumes. *Long Waves Symposium, Thessaloniki, Greece, 2003*. In Parallel with XXX IAHR Congress.
- Schäffer, H.A., Steenberg, C.M., 2003. Second-order wavemaker theory for multidirectional waves. *Ocean Engineering* 30, 1203–1231.
- Watts, S., 1999. Hybrid hydrodynamic modelling. *Journal of Offshore Technology* 7 (1), 13–17.
- Zhang, H., Schäffer, H.A., 2004. Waves in numerical and physical wave flumes — a deterministic combination. *Proceedings of the 29th International Conference on Coastal Engineering, Lisbon, Portugal, Sept., 2004*.
- Zhang, H., Schäffer, H.A., 2005. Waves in numerical and physical wave basins — a deterministic combination. *Proceedings of Waves 2005, Madrid, Spain, July, 2005*.
- Zhang, H., Schäffer, H.A., in press. Approximate Stream Function wavemaker theory for highly non-linear waves in wave flumes. *Ocean Engineering*.